INFERRING HIGHER-ORDER INTERACTIONS FROM DYNAMICS VIA HODGE-BASED MESSAGE PASSING

Anonymous authors
Paper under double-blind review

ABSTRACT

Higher-order networks represent group interactions that shape collective dynamics. The joint influence of pairwise and higher-order interactions on node evolution makes inferring these structures from observed node states challenging. In this work, we propose SCHOD (Simplicial Complex Inference with Hodge-based Dynamic Modeling), a framework for jointly inferring pairwise and 2-simplex interactions without prior knowledge of the underlying dynamical equations. The Hodge 1-Laplacian captures lower- and higher-order relations among edges in a simplicial complex. SCHOD builds on this property by incorporating learnable structural probabilities into its lower and upper components, enabling edge-to-edge message passing for structure inference. To account for node-level variation in the contributions of pairwise and 2-simplex interactions, an adaptive gating mechanism modulates their aggregated messages for state prediction. Experiments on synthetic networks demonstrate the effectiveness of SCHOD in recovering higher-order interactions across different network types.

1 INTRODUCTION

Graphs are widely used to represent complex systems, with nodes denoting entities and edges encoding pairwise interactions. However, an entity's evolution may depend jointly on multiple other entities. Such collective interactions cannot be fully captured by pairwise relationships alone, motivating representations that explicitly model higher-order interactions (Battiston et al., 2020). Higher-order networks extend pairwise graphs by explicitly representing interactions among more than two entities, which commonly arise in domains including neuroscience (Yu et al., 2011), chemistry (Cencetti et al., 2021), and ecological systems (Grilli et al., 2017). Two widely used mathematical representations of higher-order interactions are hypergraphs and simplicial complexes. Unlike general hypergraphs, simplicial complexes satisfy the closure property, whereby every simplex is accompanied by all its lower-dimensional faces (Ghorbanchian et al., 2021). This property provides a consistent representation of interactions across different orders. In real-world systems, the underlying structures often remain unknown, whereas node states can be observed through system dynamics. Inferring these hidden structures from observed dynamics constitutes a classical inverse problem in complex system modeling.

Existing studies have proposed various methods for recovering hidden interaction structures from observed dynamics. Kipf et al. (2018) introduced Neural Relational Inference (NRI), a variational autoencoder-based framework that learns latent graph structures from node trajectories in an unsupervised manner and predicts future dynamics based on the inferred interactions. However, NRI is primarily designed for pairwise relationships and cannot characterize group interactions. Recent studies have extended structure reconstruction beyond pairwise graphs to higher-order interactions. Many existing approaches rely on prior knowledge of governing equations or predefined interaction functions to identify higher-order structures (Malizia, 2024). A few model-free approaches relax the dependence on explicit dynamical equations, but they still require specific assumptions on observed data. These limitations motivate the development of a general structure inference framework capable of jointly recovering interactions across different orders without restrictive prior assumptions.

To address this challenge, we focus on simplicial complexes as the representation of higher-order interaction structures. Hodge theory provides a natural mathematical framework to characterize such dependencies by introducing lower- and upper-dimensional operators, which capture the coupling

Reviewers: please read the Reviewer Guidelines (iclr.cc/Conferences/2027/ReviewerGuidelines) and the AI Policy for Reviewers (iclr.cc/Conferences/2027/AIPolicyForReviewers). If you used AI to expand, edit, or polish your review, please provide the input text to the LLM. Better still, consider skipping the LLM and submitting your original text: we, and the authors, are much more interested in your unedited thoughts than in what an LLM has to say. AI-assisted or not, you are putting your name and reputation behind your review: LLM-generated falsehoods, hallucinations or misrepresentations are subject to disciplinary action, which may include desk-rejecting all papers you have authored.

among interactions within simplicial complexes. Based on this perspective, we propose SCHOD (Simplicial Complex Inference with Hodge-based Dynamic Modeling), a framework that jointly infers pairwise and 2-simplex interactions from observed node states. SCHOD incorporates learnable structural probabilities into Hodge-based edge-to-edge message passing to capture dependencies among interactions. Furthermore, we employ an adaptive gating mechanism to dynamically balance the node-level messages aggregated from the pairwise and 2-simplex interaction branches during state evolution.

The main contributions of this work are summarized as follows:

- We propose SCHOD, a framework for jointly inferring pairwise and 2-simplex interactions from observed node dynamics, without requiring knowledge of the governing dynamical equations.
- We introduce Hodge-based edge-to-edge message passing that uses lower and upper adjacency within a unified mechanism to propagate information through shared nodes and 2-simplices.
- We introduce an adaptive gating mechanism that weights the pairwise and 2-simplex prediction branches when predicting future node states.

2 Related Work

Pairwise Network Reconstruction. Network reconstruction aims to infer hidden interaction structures from observed data. Classical statistical and information-theoretic approaches include Granger causality (Granger, 1969), causation entropy (Sun et al., 2015), and transfer entropy (Schreiber, 2000). More recently, deep learning methods, exemplified by NRI (Kipf et al., 2018), have learned latent interaction structures in an unsupervised manner by predicting future node states from observed trajectories. Subsequent studies have extended relational inference to broader settings. dNRI (Graber & Schwing, 2020) models temporally evolving interactions, RAIN (Li et al., 2021) infers continuous interaction strengths, and ORI (Kang et al., 2024) updates latent graphs online from streaming observations. Other studies focus on improving the inference mechanism. iSIDG (Wang & Pang, 2022) iteratively refines directed interaction graphs, while IPSI (Gong et al., 2026) guides structural refinement using automatically inferred priors. Nevertheless, these methods consider only pairwise relations, leaving higher-order interactions outside their original problem settings.

Higher-Order Network Reconstruction. Higher-order network structures are difficult to infer from observed node states alone, as changes in these states can reflect the combined effects of pairwise and higher-order interactions. Some reconstruction methods therefore rely on prior knowledge of how interactions of different orders enter the dynamics. For example, Wang et al. (2022) reconstruct simplicial complexes from binary observations under simplicial contagion and Ising dynamics. Other methods formulate higher-order reconstruction as a parameter identification problem under known governing equations. Malizia (2024), Zang et al. (2024), and Fan & Wu (2022) recover higher-order structures by estimating unknown interaction parameters within predefined dynamical models, which requires prior knowledge of the underlying equations. Model-free reconstruction has also been explored to reduce the reliance on prior dynamical knowledge. ARNI (Casadiego et al., 2017) and THIS (Delabays et al., 2025) infer higher-order interactions through predefined nonlinear basis libraries without requiring explicit dynamical equations, making their performance dependent on the selected basis functions. They also impose specific data requirements, with ARNI requiring sufficiently fine temporal sampling for derivative estimation and THIS relying on observations collected within an appropriate state-space region for accurate Taylor approximation. Nevertheless, a general framework for directly learning pairwise and higher-order interaction structures from observed dynamics without explicit knowledge of the governing equations is still lacking.

3 PRELIMINARIES

3.1 SIMPLICIAL COMPLEXES

A simplicial complex (SC) is a mathematical structure composed of simplices of different orders, which provides a natural representation for higher-order networks. Specifically, a k-simplex is defined as a set of $k+1$ vertices; for example, a 0-simplex represents a node, a 1-simplex represents an edge, and a 2-simplex represents a triangle. For a k-simplex, any $(k-1)$-simplex contained in it is called a face, while any $(k+1)$-simplex containing it is referred to as a coface. A simplicial complex X has the closure property that, for any k-simplex $S_k \in X$, all faces of S_k are also included in X(Huang et al., 2024). The order of an SC is defined by the maximum order of its simplices. For simplicity, we focus on simplicial complexes of dimension two, containing N 0-simplices (nodes), $|\mathcal{E}|$ 1-simplices (edges), and $|\mathcal{S}|$ 2-simplices.

3.2 HODGE LAPLACIANS

The k-th incidence matrix $B_k \in \mathbb{R}^{N_{k-1}\times N_k}$, where N_k is the number of k-simplices, records the incidence relations between oriented k-simplices and their $(k-1)$-dimensional faces. Its entries belong to $\{-1, 0, 1\}$ (Yang et al., 2022). For simplicial complexes up to order 2, we focus on the node–edge incidence matrix $B_1 \in \mathbb{R}^{N\times|\mathcal{E}|}$ and the edge–simplex incidence matrix $B_2 \in \mathbb{R}^{|\mathcal{E}|\times|\mathcal{S}|}$. Each column of B_1 assigns -1 and $+1$ to the source and target nodes of an oriented edge, respectively. The signs in each column of B_2 are determined by the oriented boundary of the corresponding 2-simplex. For an oriented 2-simplex $[i, j, k]$, its boundary is

$$\partial[i, j, k] = [j, k] - [i, k] + [i, j], \tag{1}$$

which assigns $+1$, -1, and $+1$ to its three boundary edges, respectively, and 0 to all other edges.

Given the incidence matrices defined above, the Hodge k-Laplacian is defined as

$$L_k = \underbrace{B_k^\top B_k}_{L_k^\ell} + \underbrace{B_{k+1}B_{k+1}^\top}_{L_k^u}, \qquad 0 \le k \le K, \tag{2}$$

where $B_0 = 0$ and $B_{K+1} = 0$ by convention. As a special case, $L_0 = B_1 B_1^\top$ corresponds to the conventional graph Laplacian of a pairwise network and acts on node-level signals. For simplicial complexes up to order 2, the Hodge 1-Laplacian $L_1 = B_1^\top B_1 + B_2 B_2^\top$ acts on edge-level signals, where the two terms encode lower- and upper-level interactions, respectively (Huang et al., 2025). The lower component L_1^ℓ encodes edge relationships induced by shared nodes, whereas the upper component L_1^u encodes edge relationships induced by shared 2-simplices.

4 METHOD

4.1 PROBLEM FORMULATION

Consider a simplicial complex consisting of N nodes with a maximum order of two, whose structure consists of pairwise and 2-simplex interactions. We observe the d-dimensional states of N nodes over T time steps, denoted as $\mathbf{X} = \{\mathbf{x}_i^t\}_{i,t=1}^{N,T}$, where $\mathbf{x}_i^t \in \mathbb{R}^d$ represents the state of node i at time t. Given these observed trajectories, we aim to infer the latent simplicial structure that governs the system dynamics. We decompose the simplicial complex into pairwise interactions and 2-simplex interactions. An adjacency matrix $\mathbf{A} \in \{0, 1\}^{N\times N}$ represents the pairwise interactions, where $A_{ij} = 1$ indicates a direct interaction between nodes i and j. A set of 2-simplices $\mathcal{S}$ represents the higher-order interactions, where each simplex $(i, j, k) \in \mathcal{S}$ indicates a triadic interaction among three nodes that cannot be fully described by three independent pairwise edges. Accordingly, the model recovers a simplicial complex $\mathcal{K} = (\mathcal{V}, \mathbf{A}, \mathcal{S})$ from observed time-series data.

SCHOD (Simplicial Complex inference with Hodge-based Dynamic Modeling) provides a data-driven framework for reconstructing pairwise and 2-simplex interactions from observed node trajectories. As shown in Fig. 1, SCHOD integrates a probabilistic relational module with a Hodge-based dynamic modeling module. The probabilistic relational module estimates latent interaction probabilities for pairwise and 2-simplex interactions, and the Hodge-based dynamic modeling module

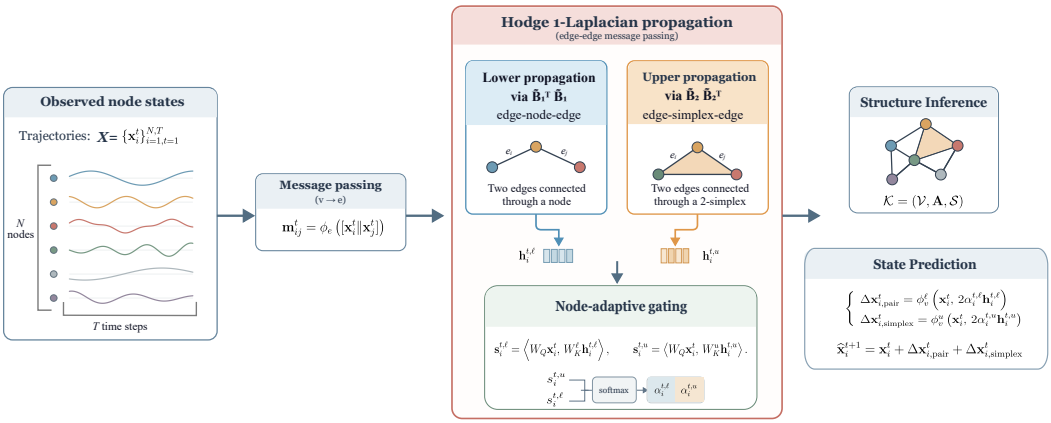


Figure 1: Overview of SCHOD. Given observed node trajectories, SCHOD constructs edge messages and propagates them through the lower and upper components of the Hodge 1-Laplacian, capturing relations between edges that share a node or belong to the same 2-simplex. Node-adaptive gating combines the resulting representations for state prediction.

uses these probabilities to construct Hodge-theoretic operators for modeling node-state evolution. To stabilize the recovery of sparse higher-order structures, SCHOD adopts a two-step training strategy. In the first step, SCHOD ignores higher-order effects and reconstructs a candidate pairwise graph. In the second step, SCHOD jointly refines pairwise edges and recovers 2-simplex interactions based on this candidate graph, which reduces the search space for higher-order structures.

4.2 Probabilistic Relational Module

We parameterize the pairwise and 2-simplex interactions using learnable logits $\boldsymbol{\pi}_{ij}^e \in \mathbb{R}^2$ and $\boldsymbol{\pi}_{ijk}^s \in \mathbb{R}^2$, respectively. Each logit vector corresponds to a binary categorical distribution, where class 0 and class 1 indicate the absence and presence of the corresponding interaction. To parameterize the discrete interaction structures in a differentiable manner, we apply the Gumbel–Softmax relaxation:

$$\mathbf{z}_{ij}^e = \mathrm{softmax}\left(\frac{\boldsymbol{\pi}_{ij}^e + \mathbf{g}_{ij}^e}{\tau}\right), \qquad \mathbf{z}_{ijk}^s = \mathrm{softmax}\left(\frac{\boldsymbol{\pi}_{ijk}^s + \mathbf{g}_{ijk}^s}{\tau}\right), \tag{3}$$

where $\mathbf{g}_{ij}^e$ and $\mathbf{g}_{ijk}^s$ denote the sampled Gumbel noises, and τ is the temperature parameter. We compute the pairwise and 2-simplex interaction existence probabilities from the presence category as $p_{ij}^e = (\mathbf{z}_{ij}^e)_1$ and $p_{ijk}^s = (\mathbf{z}_{ijk}^s)_1$, respectively.

To encourage each 2-simplex to be supported by its boundary edges, we define a geometric support factor using the minimum of the two directional pairwise assignments:

$$G_{ijk} = \left[\min\left(p_{ij}^e, p_{ji}^e\right) \min\left(p_{ik}^e, p_{ki}^e\right) \min\left(p_{jk}^e, p_{kj}^e\right)\right]^{1/3}, \qquad p_{ijk}^s \leftarrow p_{ijk}^s G_{ijk}. \tag{4}$$

During backpropagation, G_{ijk} is detached to prevent the simplex branch from updating the pairwise assignments through this factor. Hereafter, p_{ijk}^s denotes the updated assignment.

Remark (Support-level closure consistency). The updated simplex assignments satisfy support-level closure consistency:

$$p_{ijk}^s > 0 \implies \min\left(p_{ij}^e, p_{ji}^e\right) > 0, \quad \min\left(p_{ik}^e, p_{ki}^e\right) > 0, \quad \min\left(p_{jk}^e, p_{kj}^e\right) > 0. \tag{5}$$

If any boundary edge has zero inferred support in either direction, then $G_{ijk} = 0$, making the updated simplex assignment zero. This multiplicative support factor provides a soft relaxation of downward closure, without guaranteeing closure after thresholding.

4.3 HODGE-BASED DYNAMIC MODELING

Following the message-passing mechanism in graph neural networks, given the node states $\mathbf{x}_i^t$ and $\mathbf{x}_j^t$ at time t, we compute the message from node j to node i as

$$\mathbf{m}_{ij}^t = \sum_{r=0}^{1} (\mathbf{z}_{ij}^e)_r \, \phi_{e,r}\big([\mathbf{x}_i^t \| \mathbf{x}_j^t]\big) \,. \tag{6}$$

where $\phi_{e,r}(\cdot)$ is an MLP for relation type r, and $[\cdot\|\cdot]$ denotes concatenation.

Inspired by the lower and upper components of the Hodge Laplacian, we separate interaction propagation into two complementary channels. Specifically, edge representations exchange information through shared incident nodes and shared 2-simplices, corresponding to lower and upper adjacency, respectively. To condition these propagation channels on the inferred simplicial structure, we incorporate the learned pairwise and 2-simplex probabilities into the boundary matrices:

$$\widetilde{B}_1 = B_1 \operatorname{diag}\left(\sqrt{\mathbf{p}^e}\right), \qquad \widetilde{B}_2 = B_2 \operatorname{diag}\left(\sqrt{\mathbf{p}^s}\right). \tag{7}$$

To restrict message passing to distinct edges, we define the weighted lower and upper Hodge operators with their self-propagation terms removed:

$$\widetilde{L}_1^{\ell} = \widetilde{B}_1^{\top} \widetilde{B}_1 - \operatorname{Diag}\Big(\operatorname{diag}\Big(\widetilde{B}_1^{\top} \widetilde{B}_1\Big)\Big), \qquad \widetilde{L}_1^{u} = \widetilde{B}_2 \widetilde{B}_2^{\top} - \operatorname{Diag}\Big(\operatorname{diag}\Big(\widetilde{B}_2 \widetilde{B}_2^{\top}\Big)\Big), \tag{8}$$

where $\operatorname{diag}(\cdot)$ extracts the diagonal entries of a matrix and $\operatorname{Diag}(\cdot)$ constructs a diagonal matrix from a vector. We analyze the transformation properties of these operators.

Proposition 1 (Permutation Equivariance). Under consistent reindexing of nodes, edges, and 2-simplices, together with their structural probabilities and input edge representations, both weighted operators $\widetilde{L}_1^{\ell}$ and $\widetilde{L}_1^{u}$ produce correspondingly permuted edge outputs. The proof is provided in Appendix A.1.

Proposition 2 (Orientation Equivariance). Suppose the structural probabilities are independent of reference orientation. Under consistent reorientation of the boundary matrices and input edge representations, both weighted operators $\widetilde{L}_1^{\ell}$ and $\widetilde{L}_1^{u}$ produce outputs that follow the same edge reorientation. The proof is provided in Appendix A.2.

Let $\mathbf{m}^t$ collect the edge-level messages $\mathbf{m}_{ij}^t$ defined above. Based on the lower and upper components of the weighted Hodge 1-Laplacian, we propagate edge-level information through shared incident nodes and shared 2-simplices, respectively.

The edge representations produced by the lower and upper propagation channels are then given by

$$\mathbf{m}^{t,\ell} = \widetilde{L}_1^{\ell} \mathbf{m}^t, \qquad \mathbf{m}^{t,u} = \widetilde{L}_1^{u} \mathbf{m}^t. \tag{9}$$

To obtain node-level representations, the propagated edge messages are aggregated according to the unsigned node–edge incidence matrix. Specifically, the lower- and upper-channel representations of node i are

$$\mathbf{h}_i^{t,\ell} = \sum_{e=1}^{E} |B_{1,ie}| \, \mathbf{m}_e^{t,\ell}, \qquad \mathbf{h}_i^{t,u} = \sum_{e=1}^{E} |B_{1,ie}| \, \mathbf{m}_e^{t,u}, \tag{10}$$

where E denotes the number of candidate edges. Taking the absolute value removes the orientation signs while retaining the incidence relation between nodes and edges.

Nodes exhibit diverse participation patterns in pairwise edges and 2-simplices, leading to varying contributions from lower- and higher-order interactions. To balance these node-dependent contributions, we introduce a node-level adaptive gating mechanism. For node i, we measure the compatibility between its current state and each channel representation as follows:

$$s_i^{t,\ell} = \left\langle W_Q \mathbf{x}_i^t, \, W_K^{\ell} \mathbf{h}_i^{t,\ell} \right\rangle, \qquad s_i^{t,u} = \left\langle W_Q \mathbf{x}_i^t, \, W_K^{u} \mathbf{h}_i^{t,u} \right\rangle, \tag{11}$$

where W_Q, W_K^{ℓ}, and W_K^{u} are learnable projection matrices that map the node state and the two channel representations to a shared latent space. We then compute the node-specific weights as

$$\left[\alpha_i^{t,\ell}, \alpha_i^{t,u}\right] = \operatorname{softmax}\left(\left[s_i^{t,\ell}, s_i^{t,u}\right]\right), \qquad \alpha_i^{t,\ell} + \alpha_i^{t,u} = 1. \tag{12}$$

We rescale the normalized gating weights by a factor of 2 before applying them to the corresponding channel representations, preserving the original scale of both channels under equal weighting. Separate prediction functions then map the gated lower- and upper-channel representations to pairwise- and 2-simplex-induced residual state changes. We predict the next state by combining the pairwise- and 2-simplex-induced state changes as

$$\widehat{\mathbf{x}}_i^{t+1} = \mathbf{x}_i^t + \phi_v^\ell \left(\mathbf{x}_i^t, 2\alpha_i^{t,\ell} \mathbf{h}_i^{t,\ell} \right) + \phi_v^u \left(\mathbf{x}_i^t, 2\alpha_i^{t,u} \mathbf{h}_i^{t,u} \right). \tag{13}$$

4.4 Optimization Objective

Given the ground-truth states $\mathbf{x}^{t+1}$, the one-step node-state prediction error is quantified by the Gaussian negative log-likelihood (NLL). For a fixed variance σ^2, this objective is equivalent to minimizing the scaled squared error:

$$\mathcal{L}_{\mathrm{NLL}} = \frac{1}{2\sigma^2} \sum_{i=1}^{N} \left\| \widehat{\mathbf{x}}_i^{t+1} - \mathbf{x}_i^{t+1} \right\|_2^2. \tag{14}$$

To regularize the inferred interaction structures, we impose KL divergence constraints on the learned structure distributions:

$$\mathcal{L}_{\mathrm{KL}} = D_{\mathrm{KL}} \left(q_\phi(p^e) \| U_e \right) + D_{\mathrm{KL}} \left(q_\phi(p^s) \| U_s \right), \tag{15}$$

where $q_\phi(p^e)$ and $q_\phi(p^s)$ denote the posterior distributions over pairwise and 2-simplex structures, respectively, and U_e and U_s represent the corresponding uniform priors.

We use an auxiliary sparsity regularizer to encourage sparse network structures comprising pairwise and 2-simplex interactions:

$$\mathcal{L}_{\mathrm{sparse}} = \|p^e\|_1 + \|p^s\|_1. \tag{16}$$

The overall training objective combines the prediction loss with KL and sparsity regularization to jointly learn the pairwise and higher-order simplicial structures and the underlying dynamics,

$$\mathcal{L} = \mathcal{L}_{\mathrm{NLL}} + \mathcal{L}_{\mathrm{KL}} + \lambda_{\mathrm{sparse}} \mathcal{L}_{\mathrm{sparse}}, \tag{17}$$

where $\lambda_{\mathrm{sparse}} = 0.4$ unless otherwise specified.

4.5 Two-step Training Procedure

Recovering both pairwise interactions and higher-order simplicial structures directly from dynamics involves a large combinatorial search space, as the number of possible 2-simplices increases rapidly with the number of nodes. To reduce the search complexity, we adopt a two-stage reconstruction procedure that first estimates a pairwise interaction skeleton by temporarily ignoring higher-order interactions, and subsequently reconstructs the complete simplicial structure, including both pairwise interactions and 2-simplices, within the reduced candidate space.

We begin with a pairwise-only reconstruction, where the higher-order interaction term is removed and the dynamics prediction is formulated as

$$\widehat{x}_i^{t+1} = x_i^t + \Delta x_{i,\mathrm{pair}}^t. \tag{18}$$

We construct the candidate skeleton by pruning unreliable interactions from the learned pairwise interaction probabilities. Specifically, we remove edges with inferred probabilities below 0.5 and fix their corresponding pairwise interaction parameters to zero in the second-stage training. The resulting graph serves as the candidate skeleton for subsequent reconstruction.

Based on this candidate skeleton graph, we define a reduced search space for the second-stage reconstruction. Within this space, the retained pairwise interactions provide a reliable initialization for further optimization, while 2-simplices involving removed edges are excluded, as a 2-simplex can only exist when three of its constituent edges are present. We then jointly optimize the remaining pairwise interactions and 2-simplices using the proposed Hodge-based dynamic modeling framework.

5 EXPERIMENTS

5.1 GENERAL SETTINGS

Network Structures. We conduct experiments on synthetic simplicial networks with three representative network structures: Erdős–Rényi (ER), Barabási–Albert (BA), and Small-World (SW) networks. In network generation, k_1 and k_2 denote the average first-order and second-order degrees, respectively. We set $k_1 = 6$ and $k_2 = 1$ for all experimental networks. Detailed network generation procedures are provided in Appendix B.1.

Dynamical Systems. The node states are generated by two dynamical systems: the higher-order Kuramoto model and higher-order susceptible–infected–susceptible (SIS) dynamics.

For the Kuramoto system, each node is associated with a four-dimensional observation vector:

$$\mathbf{x}_i(t) = \left[\dot{\theta}_i(t), \sin(\theta_i(t)), \theta_i(t), \omega_i\right], \tag{19}$$

where $\dot{\theta}_i(t)$ denotes the instantaneous phase velocity, $\theta_i(t)$ represents the oscillator phase, and ω_i is the intrinsic frequency. All four state channels are rescaled to lie within the range $[-1, 1]$. The SIS system is a classical discrete epidemic dynamics model, where each node state represents either the susceptible (0) or the infected (1). Detailed formulations of the dynamical systems are provided in Appendix B.2.

Baselines. We compare SCHOD with representative methods for relational and higher-order structure inference:

- THIS (Delabays et al., 2025): a Taylor-expansion-based approach that reconstructs interaction structures by exploiting local approximations of the underlying dynamics.
- EM-based (Wang et al., 2022): a statistical inference method that reconstructs 2-simplicial complexes from binary contagion and Ising time series using expectation maximization.
- NRI (Kipf et al., 2018): a representative model for relational inference. We adapt the original pairwise interaction inference framework to higher-order networks.

Evaluation Metrics. We evaluate structural inference performance using AUROC and AUPRC, which measure the agreement between the inferred interaction probabilities and the corresponding binary ground-truth labels. The two metrics are computed separately for pairwise interactions and 2-simplices. Results for NRI and SCHOD are reported as mean $\pm$ standard deviation over five seeds. On a fixed dataset, THIS and the EM-based method yield identical results across repeated runs.

Implementation Details. We train SCHOD on an NVIDIA GeForce RTX 4090 GPU (24 GB) using Adam with a batch size of 128. We set the initial learning rate to 5×10^{-4} for the model parameters and 0.4 for both the pairwise and 2-simplex relation variables. A StepLR scheduler halves the learning rates every 200 epochs. Training proceeds in two stages. The first stage randomly initializes the pairwise relation probabilities and learns pairwise interactions alone. The second stage uses the pairwise relations learned in the first stage as initialization and jointly learns pairwise and 2-simplex interactions. The dataset size is denoted as $a \times b$, where a and b indicate the number of trajectories and sampled time steps per trajectory, respectively. The training-validation-test split ratio is $3 : 1 : 1$.

Structure Recovery. Table 1 reports structural recovery results across network topologies and dynamical systems. SCHOD outperforms the adapted NRI baseline and the applicable dynamics-specific baseline—THIS for Kuramoto and the EM-based method for SIS—in both AUROC and AUPRC. Under Kuramoto dynamics, its 2-simplex AUPRC remains above 99% on BASC-50. Under SIS dynamics, SCHOD also achieves strong recovery, particularly for 2-simplices. These results demonstrate its ability to infer pairwise and higher-order interactions across different dynamical systems.

THIS relies on a local Taylor expansion, and the characteristics of our observed time series may limit the estimation of coefficients needed to distinguish interaction orders, contributing to its weaker performance. In Appendix C, we describe the adapted NRI baseline, THIS, and the EM-based method, and further evaluate THIS on data generated with the phase shifts required for its reconstruction.

Table 1: Structural recovery on ERSC-50, BASC-50, and SWSC-50 simplicial complexes with average degrees $k_1 = 6$ and $k_2 = 1$. The training, validation, and test sets are split in a 3:1:1 ratio. Results are evaluated by AUROC and AUPRC (%).

Method	Interaction	ERSC-50		BASC-50		SWSC-50	
		AUROC	AUPRC	AUROC	AUPRC	AUROC	AUPRC
Kuramoto (150×10)							
NRI	Pairwise	$\mathbf{100.0 \pm 0.0}$	$\mathbf{100.0 \pm 0.0}$	$\mathbf{100.0 \pm 0.0}$	$\mathbf{99.8 \pm 0.1}$	$\mathbf{100.0 \pm 0.0}$	$\mathbf{100.0 \pm 0.0}$
	2-simplex	99.8 ± 0.1	32.1 ± 15.5	99.9 ± 0.1	44.5 ± 22.7	99.8 ± 0.1	20.1 ± 10.6
THIS	Pairwise	52.4	18.0	60.3	18.3	62.4	24.8
	2-simplex	52.8	0.1	54.6	0.2	58.2	0.2
SCHOD	Pairwise	$\mathbf{100.0 \pm 0.0}$	$\mathbf{100.0 \pm 0.0}$	99.9 ± 0.2	$\mathbf{99.8 \pm 0.3}$	$\mathbf{100.0 \pm 0.0}$	$\mathbf{100.0 \pm 0.0}$
	2-simplex	$\mathbf{100.0 \pm 0.0}$	$\mathbf{99.0 \pm 0.9}$	$\mathbf{100.0 \pm 0.0}$	$\mathbf{99.2 \pm 0.6}$	$\mathbf{100.0 \pm 0.0}$	$\mathbf{97.6 \pm 1.5}$
SIS (100×10)							
NRI	Pairwise	96.9 ± 1.8	89.2 ± 11.1	95.1 ± 7.9	85.4 ± 23.5	99.1 ± 0.5	98.0 ± 0.6
	2-simplex	99.5 ± 0.9	66.6 ± 39.4	98.6 ± 2.7	44.0 ± 30.5	99.5 ± 0.8	51.9 ± 44.4
EM-based	Pairwise	94.9	88.0	**96.7**	**92.1**	98.2	95.0
	2-simplex	**100.0**	90.1	**100.0**	92.7	**100.0**	89.4
SCHOD	Pairwise	$\mathbf{99.6 \pm 0.5}$	$\mathbf{98.3 \pm 2.8}$	96.1 ± 4.8	91.8 ± 10.5	$\mathbf{99.8 \pm 0.5}$	$\mathbf{99.2 \pm 1.7}$
	2-simplex	$\mathbf{100.0 \pm 0.0}$	$\mathbf{100.0 \pm 0.0}$	99.5 ± 1.0	$\mathbf{99.1 \pm 1.9}$	$\mathbf{100.0 \pm 0.0}$	$\mathbf{100.0 \pm 0.0}$

5.2 Effect of Network Size and Data Volume

We investigate how the number of training trajectories affects structural recovery as network size increases. Figure 2 reports pairwise-edge and 2-simplex recovery for networks with different numbers of nodes and training samples. Pairwise recovery remains relatively stable, with both AUROC and AUPRC approaching one as the number of training trajectories grows. In contrast, 2-simplex recovery is more sensitive to data availability, especially on larger networks. For the 100-node network, 2-simplex AUPRC remains near zero with up to 125 training trajectories but rises sharply as more trajectories become available. These results indicate that larger networks require more training data for reliable higher-order structure inference.

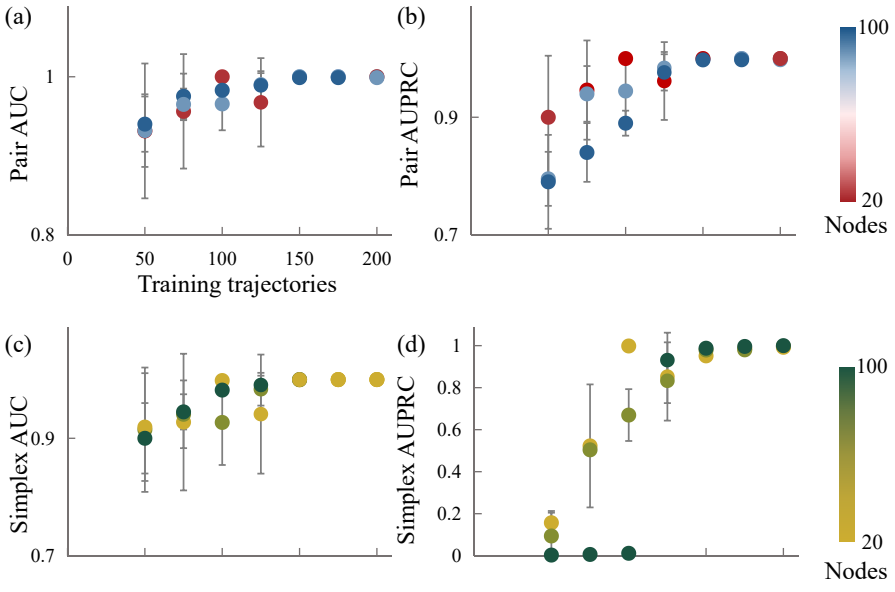


Figure 2: Structural inference with varying numbers of training trajectories (10 time steps each). Panels (a,b) show AUROC and AUPRC for pairwise interactions; panels (c,d) show the same for 2-simplex interactions. Colors denote 20, 50, and 100 nodes.

5.3 Ablation Study

Ablation of Model Components. We ablate Hodge-based message passing and adaptive gating on BASC-50 under Kuramoto dynamics, using 150×10 training datas. The w/o Hodge variant models interactions directly from node-state pairs and triplets; w/o Gate removes adaptive gating; and w/o Hodge & Gate removes both components.

As shown in Table 2, pairwise recovery remains high across all variants, while the full model achieves the highest 2-simplex AUPRC on BASC-50. Hodge-based propagation relates edges through shared nodes and 2-simplices, while adaptive gating adjusts the contributions of the two prediction branches. The ablation results indicate that both components help distinguish higher-order interactions in the observed dynamics.

Table 2: Ablation on BASC-50 under Kuramoto dynamics. AUROC and AUPRC are reported in %.

Model variant	Pairwise		2-simplices	
	AUROC	AUPRC	AUROC	AUPRC
w/o Hodge & Gate	99.97 ± 0.01	99.81 ± 0.08	99.94 ± 0.05	72.03 ± 17.06
w/o Hodge	99.98 ± 0.01	99.87 ± 0.04	99.98 ± 0.01	85.72 ± 3.15
w/o Gate	99.99 ± 0.01	99.90 ± 0.05	$\mathbf{100.00 \pm 0.00}$	96.02 ± 1.81
Full	99.00 ± 0.00	$\mathbf{99.98 \pm 0.02}$	$\mathbf{100.00 \pm 0.00}$	$\mathbf{99.20 \pm 0.66}$

Hyperparameter Sensitivity. We evaluate the sensitivity of SCHOD to the learning rate for the latent interaction variables and the sparsity weight on BASC-50 under Kuramoto dynamics. As shown in Table 3, pairwise recovery remains stable across the tested settings. 2-simplex recovery degrades markedly when the learning rate is too high, while it is less sensitive to the sparsity weight.

Table 3: Parameter sensitivity on BASC-50 under Kuramoto dynamics. AUROC and AUPRC are reported as percentages.

Parameter	Value	Pairwise		2-simplices	
		AUROC	AUPRC	AUROC	AUPRC
`lr`	0.05	100.00 ± 0.00	99.97 ± 0.03	99.98 ± 0.01	90.07 ± 6.48
	0.10	99.89 ± 0.20	99.78 ± 0.36	99.99 ± 0.01	93.26 ± 5.15
	0.20	99.88 ± 0.19	99.77 ± 0.33	100.00 ± 0.00	98.05 ± 0.98
	0.40	100.00 ± 0.00	99.97 ± 0.01	100.00 ± 0.00	$\mathbf{99.79 \pm 0.21}$
	0.80	99.88 ± 0.19	99.76 ± 0.33	99.95 ± 0.03	71.37 ± 16.95
λ_{sparse}	0.05	99.89 ± 0.20	99.78 ± 0.36	100.00 ± 0.00	97.42 ± 0.92
	0.10	100.00 ± 0.00	99.97 ± 0.02	100.00 ± 0.00	97.13 ± 2.04
	0.20	99.88 ± 0.19	99.77 ± 0.33	100.00 ± 0.00	98.05 ± 0.98
	0.40	99.89 ± 0.19	99.79 ± 0.33	100.00 ± 0.00	$\mathbf{98.40 \pm 0.89}$
	0.80	99.89 ± 0.19	99.79 ± 0.34	100.00 ± 0.00	97.02 ± 1.31

6 Conclusion and Limitations

We presented SCHOD for jointly inferring pairwise and 2-simplex interactions from observed node states. SCHOD incorporates learned interaction probabilities into Hodge-based operators, enabling edge-to-edge message passing through shared nodes and 2-simplices. An adaptive gating mechanism combines the pairwise and 2-simplex contributions to predict changes in node states. Experiments across different network topologies and dynamical systems demonstrate the effectiveness of SCHOD in recovering pairwise and 2-simplex interactions.

A limitation of SCHOD is the cost of enumerating candidate 2-simplices, which grows as $O(N^3)$ with the number of nodes. Although two-step training reduces the 2-simplex search space, SCHOD is currently limited to systems with up to 100 nodes. Future work will explore more efficient candidate selection to scale the method to larger networks. SCHOD currently considers only synthetic networks in its experiments. Future work will examine its application to real-world dynamical systems, such as social and contagion networks.

AI USE STATEMENT

We used generative AI tools to assist with language editing, literature discovery, feedback on research ideas and experimental design, and the formulation and checking of mathematical arguments and proofs. The authors independently reviewed the cited literature, verified the mathematical statements and proofs, and evaluated the experimental results. All AI-assisted text was revised by the authors. We take full responsibility for the content of this paper, including any text, claims, or artifacts produced with AI assistance.

REFERENCES

Federico Battiston, Giulia Cencetti, Iacopo Iacopini, Vito Latora, Maxime Lucas, Alice Patania, Jean-Gabriel Young, and Giovanni Petri. Networks beyond pairwise interactions: Structure and dynamics. *Physics reports*, 874:1–92, 2020.

Jose Casadiego, Mor Nitzan, Sarah Hallerberg, and Marc Timme. Model-free inference of direct network interactions from nonlinear collective dynamics. *Nature Communications*, 8(1):2192, 2017.

Giulia Cencetti, Federico Battiston, Bruno Lepri, and Márton Karsai. Temporal properties of higher-order interactions in social networks. *Scientific Reports*, 11(1):7028, 2021.

Robin Delabays, Giulia De Pasquale, Florian Dörfler, and Yuanzhao Zhang. Hypergraph reconstruction from dynamics. *Nature Communications*, 16(1):2691, 2025.

Ziye Fan and Xiaoqun Wu. Identifying partial topology of simplicial complexes. *Chaos: An Interdisciplinary Journal of Nonlinear Science*, 32(11), 2022.

Reza Ghorbanchian, Juan G. Restrepo, Joaquín J. Torres, and Ginestra Bianconi. Higher-order simplicial synchronization of coupled topological signals. *Communications Physics*, 4(1):120, 2021.

Zhongben Gong, Xiaoqun Wu, and Mingyang Zhou. Ipsi: Enhancing structural inference with automatically learned structural priors. *Advances in Neural Information Processing Systems*, 38: 156191–156209, 2026.

Colin Graber and Alexander G Schwing. Dynamic neural relational inference. In *2020 IEEE/CVF Conference on Computer Vision and Pattern Recognition (CVPR)*, pp. 8510–8519. IEEE, 2020.

Clive WJ Granger. Investigating causal relations by econometric models and cross-spectral methods. *Econometrica: journal of the Econometric Society*, pp. 424–438, 1969.

Jacopo Grilli, György Barabás, Matthew J. Michalska-Smith, and Stefano Allesina. Higher-order interactions stabilize dynamics in competitive network models. *Nature*, 548(7666):210–213, 2017.

Jinghan Huang, Qiufeng Chen, Pengli Zhu, Yijun Bian, Nanguang Chen, Moo K. Chung, and Anqi Qiu. HL-HGAT: Heterogeneous Graph Attention Network via Hodge-Laplacian Operator. *IEEE Transactions on Pattern Analysis and Machine Intelligence*, 47(12):11022–11039, 2025.

Yiming Huang, Yujie Zeng, Qiang Wu, and Linyuan Lü. Higher-Order Graph Convolutional Network with Flower-Petals Laplacians on Simplicial Complexes. *Proceedings of the AAAI Conference on Artificial Intelligence*, 38(11):12653–12661, 2024.

Beomseok Kang, Priyabrata Saha, Sudarshan Sharma, Biswadeep Chakraborty, and Saibal Mukhopadhyay. Online relational inference for evolving multi-agent interacting systems. *Advances in Neural Information Processing Systems*, 37:9801–9818, 2024.

Thomas Kipf, Ethan Fetaya, Kuan-Chieh Wang, Max Welling, and Richard Zemel. Neural relational inference for interacting systems. In *International conference on machine learning*, pp. 2688–2697. Pmlr, 2018.

Jiachen Li, Fan Yang, Hengbo Ma, Srikanth Malla, Masayoshi Tomizuka, and Chiho Choi. Rain: Reinforced hybrid attention inference network for motion forecasting. In *2021 IEEE/CVF International Conference on Computer Vision (ICCV)*, pp. 16076–16086. IEEE, 2021.

Federico Malizia. Reconstructing higher-order interactions in coupled dynamical systems. *Nature Communications*, 2024.

Thomas Schreiber. Measuring Information Transfer. *Physical Review Letters*, 85(2):461–464, 2000.

Jie Sun, Dane Taylor, and Erik M. Bollt. Causal network inference by optimal causation entropy. *SIAM Journal on Applied Dynamical Systems*, 14(1):73–106, 2015.

Aoran Wang and Jun Pang. Iterative structural inference of directed graphs. *Advances in neural information processing systems*, 35:8717–8730, 2022.

Huan Wang, Chuang Ma, Han-Shuang Chen, Ying-Cheng Lai, and Hai-Feng Zhang. Full reconstruction of simplicial complexes from binary contagion and Ising data. *Nature Communications*, 13(1):3043, 2022.

Maosheng Yang, Elvin Isufi, Michael T. Schaub, and Geert Leus. Simplicial Convolutional Filters. *IEEE Transactions on Signal Processing*, 70:4633–4648, 2022.

Shan Yu, Hongdian Yang, Hiroyuki Nakahara, Gustavo S. Santos, Danko Nikolić, and Dietmar Plenz. Higher-Order Interactions Characterized in Cortical Activity. *The Journal of Neuroscience*, 31(48):17514–17526, 2011.

Yingbang Zang, Ziye Fan, Zixi Wang, Yi Zheng, Li Ding, and Xiaoqun Wu. Stepwise reconstruction of higher-order networks from dynamics. *Chaos: An Interdisciplinary Journal of Nonlinear Science*, 34(7):073156, 2024.

A Equivariance of Weighted Hodge Operators

A.1 Permutation Equivariance

Proof of Proposition 1. Let P_0, P_1, and P_2 be permutation matrices acting on the nodes, edges, and 2-simplices, respectively. Under consistent reindexing with the reference orientations preserved, the boundary matrices and structural probabilities transform as

$$B_1' = P_0 B_1 P_1^\top, \qquad B_2' = P_1 B_2 P_2^\top, \tag{20}$$

and

$$\mathbf{A}' = P_1 \mathbf{A}, \qquad \mathbf{S}' = P_2 \mathbf{S}. \tag{21}$$

The corresponding weighting matrices satisfy

$$D_A' = \operatorname{diag}\Big(\sqrt{\mathbf{A}'}\Big) = P_1 D_A P_1^\top, \tag{22}$$

and

$$D_S' = \operatorname{diag}\Big(\sqrt{\mathbf{S}'}\Big) = P_2 D_S P_2^\top. \tag{23}$$

Hence, the weighted boundary matrices transform as

$$\widetilde{B}_1' = P_0 \widetilde{B}_1 P_1^\top, \qquad \widetilde{B}_2' = P_1 \widetilde{B}_2 P_2^\top. \tag{24}$$

Using $P_k^\top P_k = I$, the corresponding lower and upper matrix products satisfy

$$(\widetilde{B}_1')^\top \widetilde{B}_1' = P_1 \left(\widetilde{B}_1^\top \widetilde{B}_1\right) P_1^\top, \tag{25}$$

and

$$\widetilde{B}_2' (\widetilde{B}_2')^\top = P_1 \left(\widetilde{B}_2 \widetilde{B}_2^\top\right) P_1^\top. \tag{26}$$

Define the diagonal-removal operation as

$$\mathcal{O}(M) = M - \operatorname{Diag}(\operatorname{diag}(M)). \tag{27}$$

Simultaneously permuting the rows and columns preserves the diagonal positions, and thus

$$\mathcal{O}(P_1 M P_1^\top) = P_1 \mathcal{O}(M) P_1^\top. \tag{28}$$

The lower and upper propagation operators are defined as

$$\widetilde{L}_1^{\ell} = \mathcal{O}\Big(\widetilde{B}_1^{\top}\widetilde{B}_1\Big), \qquad \widetilde{L}_1^{u} = \mathcal{O}\Big(\widetilde{B}_2\widetilde{B}_2^{\top}\Big). \tag{29}$$

Therefore, for $c \in \{\ell, u\}$,

$$(\widetilde{L}_1^{c})' = P_1\widetilde{L}_1^{c}P_1^{\top}. \tag{30}$$

If the input edge representation transforms as $\mathbf{m}' = P_1\mathbf{m}$, then

$$(\widetilde{L}_1^{c})'\mathbf{m}' = P_1\widetilde{L}_1^{c}P_1^{\top}P_1\mathbf{m} = P_1\widetilde{L}_1^{c}\mathbf{m}. \tag{31}$$

Thus, both diagonal-removed weighted propagation operators are permutation equivariant. □

A.2 Orientation Equivariance

Proof of Proposition 2. Let $Q \in \mathbb{R}^{|\mathcal{E}|\times|\mathcal{E}|}$ and $R \in \mathbb{R}^{|\mathcal{S}|\times|\mathcal{S}|}$ be diagonal sign matrices representing changes in the reference orientations of edges and 2-simplices, respectively. Thus, $Q^2 = I_{|\mathcal{E}|}$ and $R^2 = I_{|\mathcal{S}|}$. Under these reorientations, the boundary matrices satisfy

$$B_1' = B_1Q, \qquad B_2' = QB_2R. \tag{32}$$

Since structural probabilities are independent of reference orientations, the weighted boundary matrices satisfy

$$\widetilde{B}_1' = \widetilde{B}_1Q, \qquad \widetilde{B}_2' = Q\widetilde{B}_2R. \tag{33}$$

Define the diagonal-removal operation by

$$\mathcal{O}(M) = M - \mathrm{Diag}\big(\mathrm{diag}(M)\big). \tag{34}$$

Because Q is a diagonal sign matrix, this operation satisfies

$$\mathcal{O}(QMQ) = Q\mathcal{O}(M)Q. \tag{35}$$

The lower-channel operator $\widetilde{L}_1^{\ell} = \mathcal{O}(\widetilde{B}_1^{\top}\widetilde{B}_1)$ therefore transforms as

$$(\widetilde{L}_1^{\ell})' = \mathcal{O}\Big((\widetilde{B}_1')^{\top}\widetilde{B}_1'\Big) = \mathcal{O}\Big(Q\widetilde{B}_1^{\top}\widetilde{B}_1Q\Big) = Q\widetilde{L}_1^{\ell}Q. \tag{36}$$

Similarly, for the upper-channel operator $\widetilde{L}_1^{u} = \mathcal{O}(\widetilde{B}_2\widetilde{B}_2^{\top})$, the identity $R^2 = I_{|\mathcal{S}|}$ gives

$$(\widetilde{L}_1^{u})' = \mathcal{O}\Big(\widetilde{B}_2'(\widetilde{B}_2')^{\top}\Big) = \mathcal{O}\Big(Q\widetilde{B}_2\widetilde{B}_2^{\top}Q\Big) = Q\widetilde{L}_1^{u}Q. \tag{37}$$

If the input edge representation transforms as $\mathbf{m}' = Q\mathbf{m}$, then, for $c \in \{\ell, u\}$,

$$(\widetilde{L}_1^{c})'\mathbf{m}' = Q\widetilde{L}_1^{c}Q^2\mathbf{m} = Q\widetilde{L}_1^{c}\mathbf{m}. \tag{38}$$

Thus, both diagonal-removed weighted propagation operators are orientation equivariant. □

B Data Generation

B.1 Simplicial Complex Generation

We construct three types of simplicial complexes—Erdős–Rényi (ERSC), Barabási–Albert (BASC), and Watts–Strogatz (SWSC)—as described below.

ERSC. We construct an Erdős–Rényi simplicial complex (ERSC) by independently sampling edges and 2-simplices with probabilities p_1 and p_2, respectively, where

$$p_1 = \frac{k_1 - 2k_2}{N - 1 - 2k_2}, \qquad p_2 = \frac{2k_2}{(N-1)(N-2)}. \tag{39}$$

We then add any missing simplex boundary edges to ensure downward closure.

BASC. We construct a Barabási–Albert simplicial complex (BASC) from a preferential-attachment base graph, where each new node connects to m existing nodes. We determine m by rounding

$$m^* = \frac{k_1 - 2k_2}{2(1 - 2k_2/N)} \tag{40}$$

to the nearest integer. We then independently sample 2-simplices with probability p_2 from Equation 39 and add their missing boundary edges.

SWSC. We construct a small-world simplicial complex (SWSC) from a Watts–Strogatz base graph. Each node initially connects to its $2m$ nearest neighbors on a ring, and we rewire each edge with probability 0.1. We determine m using Equation 40 and the same rounding procedure as in BASC. We then independently sample 2-simplices with probability p_2 from Equation 39 and add their missing boundary edges.

Across all experiments, we set the average degrees to $k_1 = 6$ and $k_2 = 1$. Table 4 summarizes the basic configuration of each network, including the numbers of nodes, edges, and 2-simplices.

Table 4: Network configurations with average degrees $k_1 = 6$ and $k_2 = 1$.

	ER		BA		SW	
Nodes	Edges	2-simplices	Edges	2-simplices	Edges	2-simplices
10	27	4	23	4	26	4
50	190	21	150	21	156	21
100	327	37	303	37	305	37

B.2 Dynamical Processes

B.2.1 Higher-Order Kuramoto Dynamics

We generate the dynamical data using the higher-order Kuramoto model

$$\dot{\theta}_i = \omega_i + \sum_{j=1}^{n} a_{ij} \sin(\theta_j - \theta_i) + \sum_{j,k=1}^{n} a_{ijk} \sin(\theta_j + \theta_k - 2\theta_i), \qquad i = 1, \ldots, n, \tag{41}$$

where θ_i denotes the phase of oscillator i, ω_i denotes its intrinsic frequency, and a_{ij} and a_{ijk} indicate the pairwise and 2-simplex adjacency relations, respectively. We sample the intrinsic frequencies and initial phases from $\omega_i \sim \mathcal{U}(1, 10)$ and $\theta_i(0) \sim \mathcal{U}(0, 2\pi)$, respectively. The Dormand–Prince Runge–Kutta solver (`dopri5`) integrates the ODE system with a step size of 0.01 and retains one state every 10 integration steps.

B.2.2 Higher-Order SIS Dynamics

The higher-order SIS model is a synchronous discrete-time stochastic process. Each node has a binary state $X_i(t) \in \{0, 1\}$, where 0 and 1 denote the susceptible and infected states, respectively. For a susceptible node i, the probability of remaining susceptible is

$$P_i^{0\to 0}(t) = \prod_{j=1}^{N} \left[1 - \beta_1 A_{ij} X_j(t)\right] \prod_{1 \le j < k \le N} \left[1 - \beta_2 B_{ijk} X_j(t) X_k(t)\right], \tag{42}$$

where A_{ij} denotes the pairwise adjacency and $B_{ijk} \in \{0, 1\}$ indicates whether $\{i, j, k\}$ forms a 2-simplex. The discrete-time dynamics are defined by

$$\Pr\left(X_i(t+1) = 1 \mid \mathbf{X}(t)\right) = \begin{cases} 1 - P_i^{0\to 0}(t), & X_i(t) = 0, \\ 1 - \mu, & X_i(t) = 1, \end{cases} \tag{43}$$

where β_1 and β_2 are the pairwise and 2-simplex infection probabilities, respectively, and μ is the recovery probability. All nodes are updated synchronously based on their states at time t. We set $\beta_1 = 0.15$, $\beta_2 = 0.5$, $\mu = 0.8$, and the initial infected fraction to $\rho_0 = 0.2$. Each trajectory contains 300 time steps.

C BASELINE METHODS

C.1 THIS

THIS locally expands the node dynamics using a Taylor series and applies SINDy to estimate sparse expansion coefficients. It identifies pairwise and triadic interactions from nonzero coefficients involving different nodes. Estimating these local coefficients depends on the distribution of states around the expansion point. In the Kuramoto demonstration of the original paper, states were sampled within a small region around zero, and derivatives were computed directly from the dynamical equations.

In our main experiment, we provide THIS with the same Kuramoto trajectories as the other methods to ensure a fair comparison under identical observations. The lower recovery performance in this setting may be related to the local Taylor approximation used by THIS, whose ability to identify triadic interactions depends on whether the corresponding mixed Taylor coefficients provide sufficient signals.

We conduct a separate supplementary experiment using THIS's data-generation procedure. Phase shifts are introduced into the Kuramoto dynamics used to generate the time series:

$$\dot{\theta}_i = \omega_i + \sum_{j=1}^{n} A_{ij}^{(2)} \sin(\theta_j - \theta_i + \phi_2) + \sum_{j,k=1}^{n} S_{ijk}^{(3)} \sin(\theta_j + \theta_k - 2\theta_i + \phi_3). \tag{44}$$

where ϕ_2 and ϕ_3 affect the pairwise and triadic coupling terms, respectively. These parameters belong to the data-generating dynamics rather than THIS itself.

Since the recovery of triadic interactions in THIS relies on nonzero mixed Taylor coefficients, we set $\phi_2 = 0$ and $\phi_3 = \pi/2$ to provide informative higher-order signals for the reconstruction. Under this phase configuration, we generate Kuramoto trajectories and evaluate structural recovery on ERSC-50, BASC-50, and SWSC-50 simplicial complexes using the same 150×10 trajectory setting. As shown in Table 5, THIS achieves accurate recovery of both pairwise and 2-simplex interactions, indicating that its performance depends on the local Taylor expansion signals induced by the underlying dynamics.

Table 5: Structural recovery performance of THIS on Kuramoto trajectories generated with $\phi_2 = 0$ and $\phi_3 = \pi/2$. Results are evaluated using AUROC and AUPRC (%) for pairwise and 2-simplex interactions on ERSC-50, BASC-50, and SWSC-50.

Network	Interaction type	AUROC (%)	AUPRC (%)
ERSC-50	Pairwise	100.00	100.00
ERSC-50	2-simplex	99.21	98.34
BASC-50	Pairwise	100.00	100.00
BASC-50	2-simplex	100.00	100.00
SWSC-50	Pairwise	100.00	100.00
SWSC-50	2-simplex	99.20	92.50

C.2 EM-BASED RECONSTRUCTION

The EM-based reconstruction method is a statistical inference framework for reconstructing 2-simplicial complexes from binary time-series data generated by higher-order SIS dynamics. The method formulates the reconstruction problem as a maximum likelihood estimation problem, where the probabilities of pairwise interactions and 2-simplex interactions are jointly inferred from observed state transitions. Specifically, it estimates the likelihood of a node being influenced by another node through pairwise connections and by two nodes through higher-order interactions, and optimizes these latent interaction probabilities using an expectation-maximization (EM) algorithm.

C.3 ADAPTED NRI BASELINE

We extend Neural Relational Inference (NRI) to infer both pairwise edges and 2-simplices. The relational inference procedure follows that of SCHOD and produces the relation variables $\mathbf{z}_{ij}^e$ and $\mathbf{z}_{ijk}^s$ described in Section 4.2. The adapted NRI baseline uses an MLP decoder with separate message functions for each relation type and interaction order.

For pairwise interactions, the message from node j to node i is

$$\mathbf{m}_{ij}^{e,t} = \sum_{r=0}^{1} (\mathbf{z}_{ij}^e)_r \, \phi_{e,r}\big([\mathbf{x}_i^t \| \mathbf{x}_j^t]\big) \,. \tag{45}$$

Node i aggregates its incoming pairwise messages and predicts the corresponding state increment:

$$\mathbf{M}_i^{e,t} = \sum_{j \neq i} \mathbf{m}_{ij}^{e,t}, \qquad \Delta\mathbf{x}_{i,\text{pair}}^t = \phi_v^e\big([\mathbf{x}_i^t \| \mathbf{M}_i^{e,t}]\big) \,. \tag{46}$$

For three-node interactions, the message associated with an ordered triplet (i, j, k), where i is the receiving node, is

$$\mathbf{m}_{ijk}^{s,t} = \sum_{r=0}^{1} (\mathbf{z}_{ijk}^s)_r \, \phi_{s,r}\big([\mathbf{x}_i^t \| \mathbf{x}_j^t \| \mathbf{x}_k^t]\big) \,. \tag{47}$$

The simplex messages yield a second state increment:

$$\mathbf{M}_i^{s,t} = \sum_{j,k \neq i} \mathbf{m}_{ijk}^{s,t}. \qquad \Delta\mathbf{x}_{i,\text{simplex}}^t = \phi_v^s\big([\mathbf{x}_i^t \| \mathbf{M}_i^{s,t}]\big) \,, \tag{48}$$

where $\phi_{e,r}$ and $\phi_{s,r}$ are relation-type-specific MLPs, while ϕ_v^e and ϕ_v^s are separate output MLPs. Without node-adaptive gating, the decoder directly combines the two increments through a residual update:

$$\widehat{\mathbf{x}}_i^{t+1} = \mathbf{x}_i^t + \Delta\mathbf{x}_{i,\text{pair}}^t + \Delta\mathbf{x}_{i,\text{simplex}}^t. \tag{49}$$

D MORE RESULTS

D.1 ABLATION STUDY

Table 6: Ablation results on the SWSC-50 simplicial complex under Kuramoto dynamics, evaluated by AUROC and AUPRC (%).

Model variant	Pairwise		2-simplices	
	AUROC	AUPRC	AUROC	AUPRC
w/o Hodge & Gate	100.00 ± 0.00	99.99 ± 0.01	99.75 ± 0.08	19.65 ± 9.53
w/o Hodge	100.00 ± 0.00	100.00 ± 0.00	99.75 ± 0.07	27.91 ± 6.06
w/o Gate	$\mathbf{100.00 \pm 0.00}$	$\mathbf{100.00 \pm 0.00}$	$\mathbf{99.99 \pm 0.01}$	93.36 ± 2.81
Full	$\mathbf{100.00 \pm 0.00}$	$\mathbf{100.00 \pm 0.00}$	99.99 ± 0.00	$\mathbf{97.58 \pm 1.72}$

Table 7: Ablation results on the ERSC-50 simplicial complex under Kuramoto dynamics, evaluated by AUROC and AUPRC (%).

Model variant	Pairwise		2-simplices	
	AUROC	AUPRC	AUROC	AUPRC
w/o Hodge & Gate	99.99 ± 0.00	99.97 ± 0.01	99.86 ± 0.12	47.47 ± 28.84
w/o Hodge	99.99 ± 0.00	99.96 ± 0.02	99.88 ± 0.09	50.04 ± 22.77
w/o Gate	$\mathbf{100.00 \pm 0.00}$	$\mathbf{100.00 \pm 0.00}$	$\mathbf{99.99 \pm 0.00}$	96.30 ± 2.18
Full	$\mathbf{100.00 \pm 0.00}$	$\mathbf{100.00 \pm 0.00}$	$\mathbf{99.99 \pm 0.00}$	$\mathbf{99.02 \pm 1.04}$

Tables 6 and 7 provide additional ablation results under Kuramoto dynamics. Pairwise recovery remains strong across the variants, whereas 2-simplex recovery is more sensitive to the model components. Removing Hodge-based propagation substantially reduces 2-simplex AUPRC, supporting its role in capturing higher-order interaction structure.

D.2 Noise Robustness

To evaluate the robustness of SCHOD against observation noise, we conduct a noise robustness experiment on the Kuramoto dataset by perturbing the observations with additive Gaussian noise:

$$\widetilde{\mathbf{X}} = \mathbf{X} + \sigma\boldsymbol{\varepsilon}, \qquad \boldsymbol{\varepsilon} \sim \mathcal{N}(\mathbf{0}, \mathbf{I}), \tag{50}$$

where $\sigma \in \{0, 0.05, 0.10, 0.15, 0.20, 0.25, 0.30\}$ controls the standard deviation of the Gaussian noise added to the Kuramoto observations, and the original state values lie in the range $[-1, 1]$. The entries of $\boldsymbol{\varepsilon}$ are sampled independently, and independent noise realizations are generated for the training, validation, and test sets.

Figure 3 shows how observation noise affects pairwise-edge and 2-simplex recovery, measured by AUROC and AUPRC. Both methods maintain relatively stable performance on pairwise interaction recovery as the noise level increases, indicating that pairwise structures remain identifiable under observation perturbations. For 2-simplex recovery, the adapted NRI baseline shows a noticeable performance degradation with increasing noise, whereas SCHOD consistently achieves higher AUROC and AUPRC across different noise levels. These results demonstrate that SCHOD better preserves the recovery of higher-order interactions from noisy trajectories.

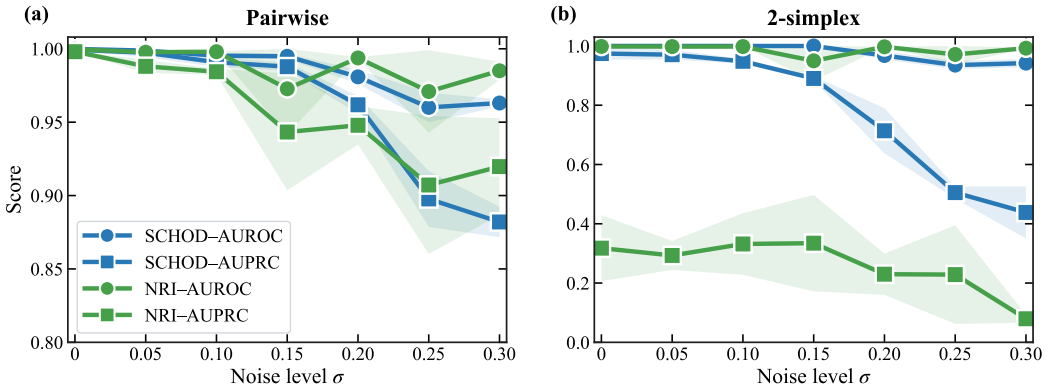


Figure 3: Effect of observation noise on pairwise and 2-simplex interaction inference. Panels (a) and (b) show the corresponding AUROC and AUPRC for SCHOD and the adapted NRI baseline.